Proceedings of the ASME 2026 45th International Conference on Ocean, Offshore and Arctic Engineering
OMAE2026
June 7-12, 2026, Tokyo, Japan

OMAE2026-181942

NUMERICAL INVESTIGATION OF SCALE EFFECTS ON CFPSO HYDRODYNAMIC RESPONSES UNDER IRREGULAR WAVES

Mingqiu Liu
Computational Marine Hydrodynamics Lab (CMHL), State Key Laboratory of Ocean Engineering, School of Ocean and Civil Engineering, Shanghai Jiao Tong University, Shanghai, China

Maokun Ye
Computational Marine Hydrodynamics Lab (CMHL), State Key Laboratory of Ocean Engineering, School of Ocean and Civil Engineering, Shanghai Jiao Tong University, Shanghai, China

Shenglei Fu
CNOOC Research Institute, Beijing, China

Decheng Wan*
Computational Marine Hydrodynamics Lab (CMHL), State Key Laboratory of Ocean Engineering, School of Ocean and Civil Engineering, Shanghai Jiao Tong University, Shanghai, China

ABSTRACT

In this study, the hydrodynamic characteristics of a cylindrical floating production storage offloading (CFPSO) at different scale ratios under irregular wave conditions are investigated using an in-house CFD solver, naoe-FOAM-SJTU. The scale effects on motion responses, horizontal loads, green water phenomena, and slamming pressure are systematically analyzed. The results indicate that the overall evolution trends of motion responses and horizontal loads exhibit good consistency across different scale ratios. The differences in time-averaged motion responses and mean horizontal loads are relatively small, while scale effects are mainly reflected in instantaneous extreme responses, with slightly higher extreme values observed for larger-scale cases. The temporal sequence of green water occurrence remains generally consistent among different scales; however, noticeable differences are observed in green water intensity and residence time. Slamming events show similar occurrence frequency and temporal distribution across different scale ratios, whereas significantly higher slamming pressures are recorded at high-elevation probes away from the free surface for larger-scale cases, with differences reaching up to 44%. The findings of this study provide a useful reference for the assessment of scale effects of CFPSOs in engineering applications.

Keywords: Cylindrical FPSO; CFD; scale effects; hydrodynamic responses

1. INTRODUCTION

Cylindrical floating production storage offloading (CFPSO) is a novel offshore oil and gas production facility[1]. Compared with conventional FPSOs, CFPSOs exhibit advantages in terms of lower construction cost and easier installation[2]. Operating in complex marine environments, CFPSOs are subjected to wave and current loads, which induce complicated hydrodynamic responses. Therefore, the investigation of hydrodynamic responses is of critical importance for the design and safe operation of CFPSOs.

The hydrodynamic responses of CFPSOs are commonly investigated using physical model experiments, potential-flow-based methods, and computational fluid dynamics (CFD). Model experiments are widely adopted during the design stage, as they provide data with relatively high reliability; however, they are usually associated with high experimental costs. Gu et al.[3] investigated the free decay behavior of an FDPSO using model experiments, from which the natural periods and nondimensional damping coefficients were obtained. Deng et al.[4] employed model tests to study the motion responses of a CFPSO under combined wave–current conditions, and the results indicated that the heave and roll motions were slightly larger than those induced by waves alone.

Numerical methods based on potential-flow theory provide an alternative approach for investigating CFPSO hydrodynamic responses, offering relatively low computational cost and high efficiency, but with limited accuracy. This limitation arises because viscous effects are neglected in conventional potential-flow theory, while corrections for viscous effects usually rely on empirical parameters, leading to unavoidable uncertainties. Deng et al.[5] applied a potential-flow method, validated through experiments, to investigate the hydrodynamic characteristics of a CFPSO under wave-only and combined wave–current conditions. Cui et al.[6] studied a novel CFPSO configuration based on three-dimensional potential-flow theory, and the results demonstrated that an annular recess could suppress resonance and improve the heave response.

CFD is another widely used approach for investigating the hydrodynamic responses of CFPSOs. This method enables the acquisition of detailed flow-field information with relatively high accuracy, although at the expense of significant computational cost. Avalos and Wanderley[7] employed CFD to investigate the effects of bilge keel width and shape on the roll motion of an FPSO. Jiang et al.[8] studied the influence of heave plate width on the heave motion of a CFPSO using CFD and proposed recommendations for heave plate optimization. Huo et al.[9] investigated the relationship between slamming pressure and wave height as well as wave celerity acting on a CFPSO using CFD. Zhao et al.[10] examined the influence of liquid filling on CFPSO motion responses under different regular wave conditions based on CFD simulations.

When investigating the hydrodynamic responses of offshore structures, scale effects represent an important issue that must be addressed in both CFD simulations and model experiments[11]. Although numerous studies have focused on scale effects in ship hydrodynamics[12–14] , investigations specifically targeting scale effects of CFPSOs remain limited. In the present study, CFD simulations are conducted for CFPSOs at four different scales subjected to irregular waves. The simulations are performed using a validated in-house solver, naoe-FOAM-SJTU, developed based on OpenFOAM. For different scales of CFPSOs, we focused on analyzing the motion responses, horizontal loads, and green water phenomena.

2. NUMERICAL SIMULATION

2.1 CFD Solver

In this study, we employ an incompressible two-phase CFD solver, naoe-FOAM-SJTU[15]. The solver is developed based on OpenFOAM and is capable of simulating the hydrodynamic responses of CFPSOs under wave conditions. The solver incorporates a six-degree-of-freedom (6-DOF) motion module, in which the rigid-body motions of the floating structure are obtained by solving the Euler equations[16]. In addition, a mooring module is included, allowing the simulation of various mooring system configurations[15]. The solver has been extensively validated in previous studies[9,10,15], and further details regarding its formulation and implementation can be found in Wang et al.[15]. To balance computational cost and efficiency, we adopt the laminar flow model in the present simulations. For wave generation, we use the third-party OpenFOAM library waves2Foam, where waves are generated and absorbed through designated wave generation and damping zones.

2.2 Numerical Setup

In this study, we use a CFPSO configuration, and a schematic view of the geometric model is shown in Fig. 1. At full scale, the draft of the model is 27 m, the center of gravity is located 0.931 m below the still water level, and the total mass is approximately 1.76 × 10^8 kg. A total of 13 mooring lines are arranged for the CFPSO, and the physical parameters of each mooring-line segment are listed in Table 1. The wave conditions are defined using irregular waves based on the JONSWAP spectrum, with a significant wave height of 13.3 m, a peak period of 15 s, and a peak enhancement factor of 2.2. When simulations with different scale ratios are performed, all physical quantities are scaled according to the Froude similarity criterion.

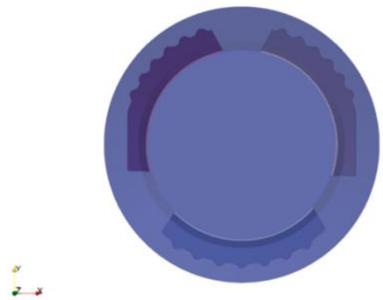

(a) top view

(b) side view

FIGURE 1: Schematic of the CFPSO geometric model

TABLE 1: Physical parameters of the mooring line segments

Segment	Length (m)	Diameter (m)	Young modulus (Pa)	Mass in water (kg/m)
Platform chain	197	0.288	3.2e10	383.5
Link	1.1	0.75	4.6e9	3500
Polyester	706.8	0.22	9.7e9	18.47
Link	2	0.74	4.8e9	4500
Anchor chain	193	0.288	2.1e9	453.2

The computational domain is illustrated in Fig. 2. The domain size is 1740 m × 720 m × 435 m, extending from (–540 m, –360 m, –315 m) to (1080 m, 360 m, 120 m). The width of the wave generation relaxation zone is 360 m, while the width of the wave absorption relaxation zone is 600 m. A sufficient number of grid cells are distributed within the wavelength and wave-height ranges to ensure the accuracy of wave propagation. Details of the mesh configuration are shown in Fig. 3, and the total number of grid cells is approximately 3.1 million. Near the free-surface boundary layer, the grid resolution is Δx = 3 m, Δy = 3 m, and Δz = 1.125 m, while the grid resolution in the vicinity of the structure is Δx = 0.75 m, Δy = 0.75 m, and Δz = 0.281 m. The above computational domain and mesh configuration correspond to the full-scale case, and the meshes for other scales are obtained by scaling according to the corresponding scale ratios. In total, four simulation cases are considered in this study, with scale ratios of 1:1, 1:20, 1:40, and 1:60. For the full-scale case, the total simulation duration is approximately 790 s, corresponding to about 52 spectral peak periods, and the time step is set to 0.1 s. For the other scale ratios, the total simulation duration is kept the same as that of the full-scale case.

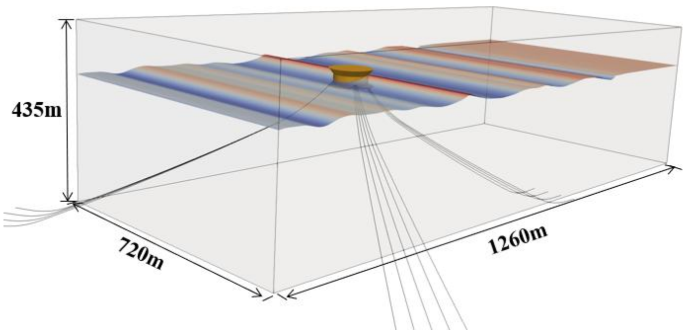

FIGURE 2: Schematic of the computational domain

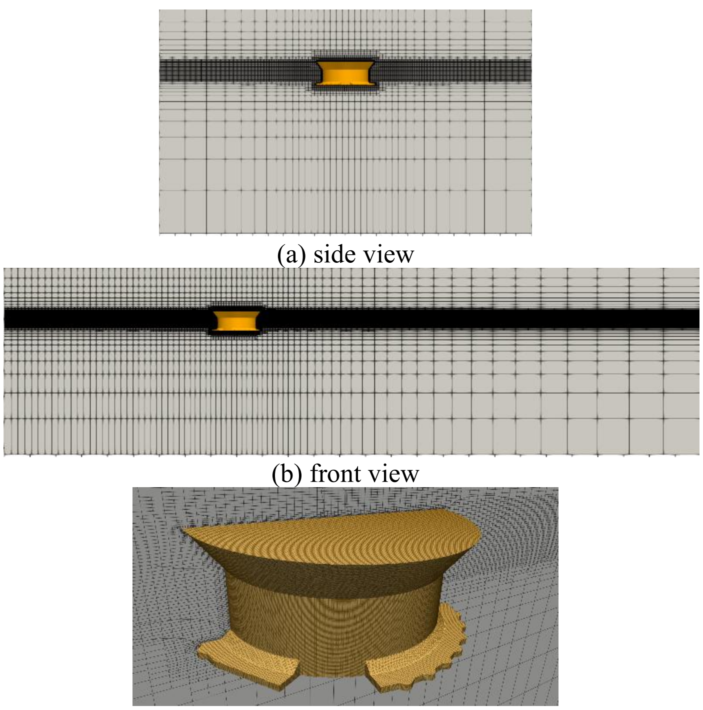

(a) side view

(b) front view

(c) mesh near the CFPSO

FIGURE 3: Schematic of the mesh configuration

2.3 Model Validation

The numerical wave-generation method is validated in this study. The irregular wave input adopted in this work is reconstructed from experimentally measured wave elevation data. To evaluate the influence of different flow-model settings on wave generation and propagation, an additional two-dimensional verification case is established without any structure in the domain. Both the experimental wave-elevation record and the two-dimensional verification are at the 1:60 model scale. The reconstructed irregular-wave input is taken from the 1:60 experimental wave-elevation record. Under identical numerical schemes, mesh, and time-step settings, the time histories of wave elevation obtained with laminar and Reynolds-Averaged Navier-Stokes (RANS) settings are compared with the experimental data. Fig. 4(a) shows the comparison of wave elevation time histories at the gauge 0 that is located near the outlet of the wave-generation zone. The results indicate that the overall differences between the laminar and RANS settings at this location are small, suggesting that the choice of flow model has a limited impact on near-field wave generation. Fig. 4(b) further compares the wave elevation time histories at the gauge 1 that is located at the reference position used for the subsequent three-dimensional CFPSO simulations. Compared with the experimental results, the laminar setting preserves the main characteristics of the wave elevation time history, whereas the RANS setting exhibits a pronounced decay in wave amplitude. This observation indicates that, within the two-phase wave-generation framework adopted in this study, RANS may introduce additional dissipation, leading to an underestimation of wave energy during propagation. Based on the above comparisons, for the reconstructed irregular-wave input considered herein, the laminar setting provides a wave environment that is more consistent with the experiments; therefore, the laminar setting is adopted for the subsequent three-dimensional scale-effect simulations.

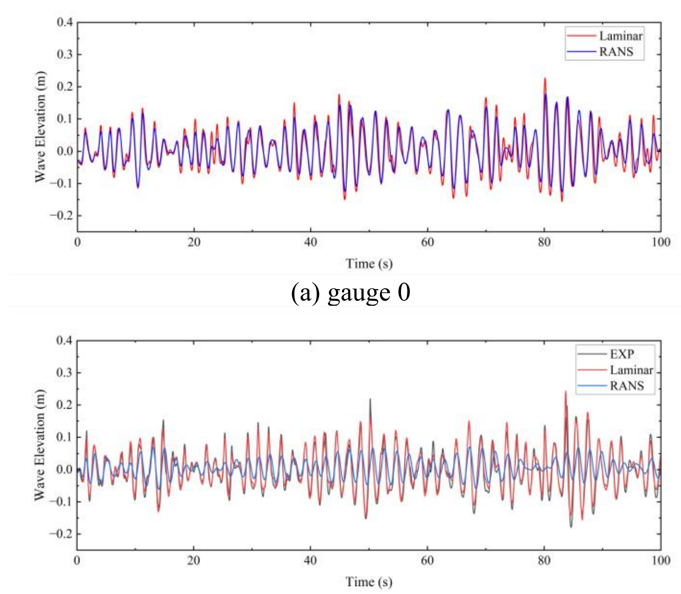

(a) gauge 0

(b) gauge 1

FIGURE 4: Comparison of wave elevation time histories for laminar and RANS

In addition, to further assess the reliability of the numerical approach, a representative regular-wave case is considered, using a wave height of 3 m and a wave period equal to the spectral peak period of the irregular wave. The RAOs of surge, heave, and pitch are compared with the experimental results, as summarized in Table 2. The results show that the motion RAOs obtained with the laminar setting agree well with the experimental data.

TABLE 2: Comparison of surge, heave, and pitch RAOs between CFD and experiment

Motion	CFD	Experiment
Surge RAO (m/m)	0.617	0.566
Heave RAO (m/m)	1.277	1.194
Pitch RAO (deg/m)	0.125	0.138

3. RESULTS AND DISCUSSION

3.1 Motion Responses

To facilitate the comparison of motion response characteristics among different scale ratios, all simulation results are scaled to the full scale according to the Froude similarity criterion. The time histories of the motion responses are presented in Fig. 5. The results show that, during the initial stage of the simulations, the motion responses have not yet reached a stable state, and relatively pronounced differences in the instantaneous responses are observed among different scale ratios. As the simulation time increases, all cases gradually enter a quasi-steady state, and the trends of the motion responses at different scales remain consistent, with smaller discrepancies than those observed during the transient stage. A comparison among different degrees of freedom indicates that the differences in heave motion across scale ratios are relatively small, suggesting that the vertical motion is insensitive to scale variation. In contrast, the surge and pitch motions exhibit more noticeable differences in their instantaneous values among different scales.

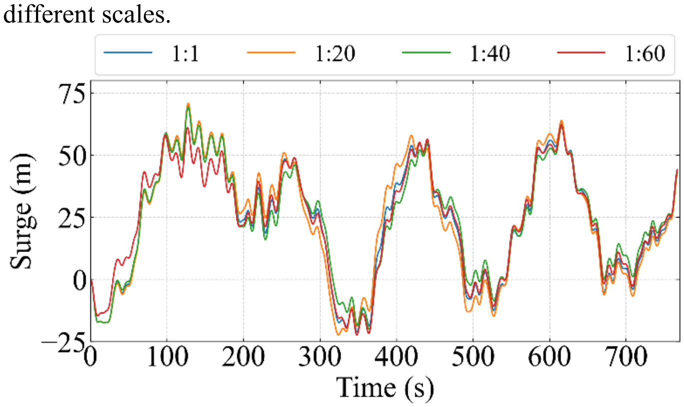

(a) surge

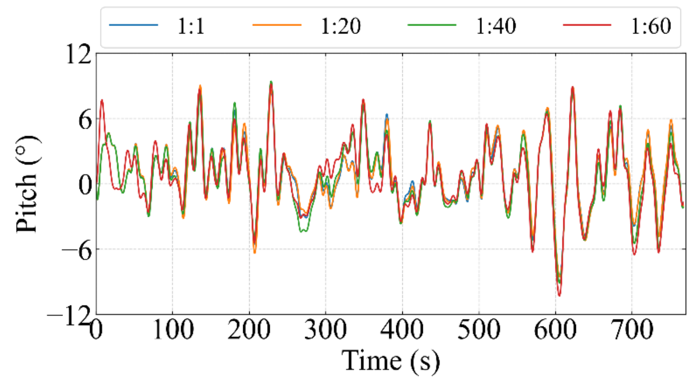

(b) pitch

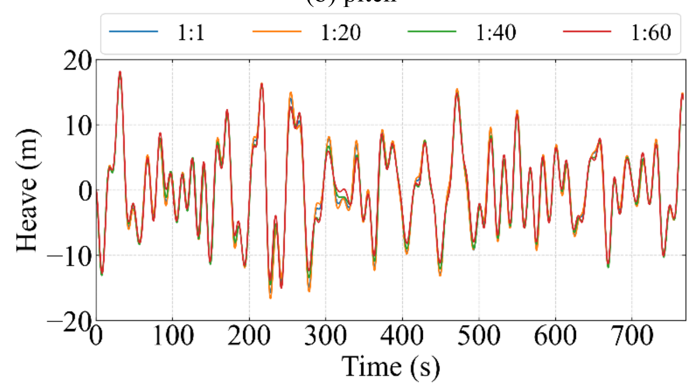

(c) heave

FIGURE 5: The time history of motion responses

The statistical values of the motion responses are further extracted and summarized in Table 3. The results show that the time-averaged motion responses exhibit only minor differences among different scale ratios, whereas relatively larger discrepancies are observed in the extreme values. Based on both the time-history and statistical analyses, it can be concluded that, under the present wave conditions, the overall motion response characteristics of CFPSOs at different scales exhibit good consistency. The scale effects are mainly manifested in the differences in the instantaneous extreme values of surge and pitch motions, while the mean responses are generally insensitive to scale variation.

TABLE 3: The statistics of motion response

Motion		1:1	1:20	1:40	1:60
surge (m)	max	70.57	70.81	69.23	62.16
	min	-21.1	-22.25	-20.01	-22.30
	mean	23.50	23.44	24.07	23.60
heave (m)	max	17.59	17.63	17.51	18.17
	min	-15.70	-16.61	-14.74	-15.03
	mean	-0.02	-0.01	-0.08	0.15
pitch (°)	max	8.88	9.03	9.41	9.14
	min	-8.51	-8.55	-9.11	-10.28
	mean	0.95	0.95	0.76	0.75

3.2 Horizontal Loads

The time histories of the horizontal loads are presented in Fig. 6, including both wave loads and mooring loads. From the time-history results, the scale dependence of the horizontal loads shows a trend similar to that observed for the motion responses. During the initial transient stage, relatively pronounced differences are observed among different scale ratios. As the simulations proceed, all cases gradually enter a statistically steady state, and the time-history trends of the horizontal loads at different scales remain consistent, with the discrepancies significantly reduced. The statistical values of the horizontal loads are summarized in Table 4. The results indicate that both the maximum and minimum horizontal loads for the 1:60 scale case are lower than those of the larger-scale cases, whereas the results for the other three scale ratios are relatively close to each other. A further comparison of the mean values reveals that the average wave loads and mooring loads for the larger-scale cases (1:1 and 1:20) are slightly higher than those for the smaller-scale cases (1:40 and 1:60). Overall, the horizontal loads exhibit a certain degree of scale dependence, with larger-scale cases generally yielding slightly higher load levels than smaller-scale cases.

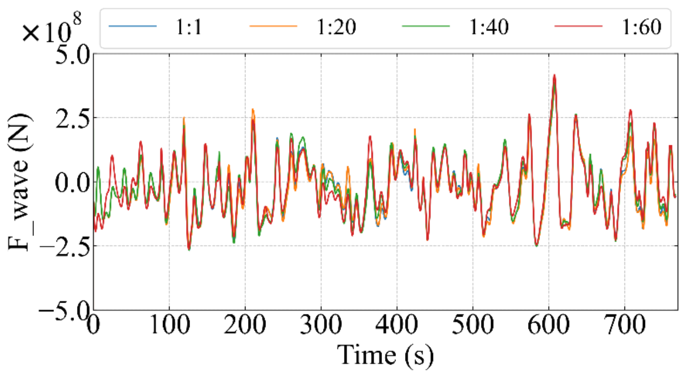

(a) wave loads

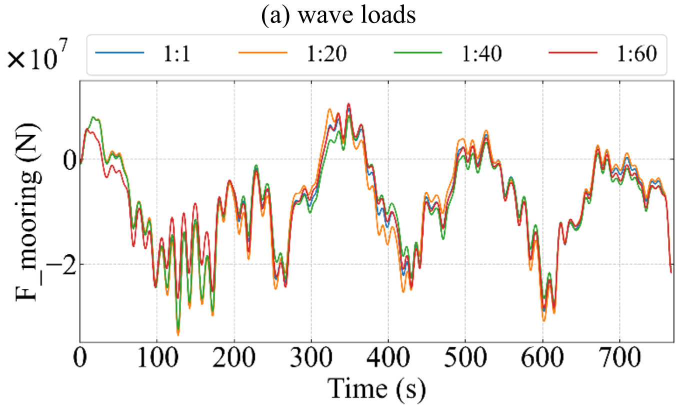

(b) mooring loads

FIGURE 6: The time history of horizontal loads

TABLE 4: The statistic of horizontal loads

Loads		1:1	1:20	1:40	1:60
wave loads (N)	max	2.8e8	3.21e8	2.19e8	2.06e8
	min	-8.96e8	-9.92e8	-7.24e8	-6.08e8
	mean	-4.19e7	-4.26e7	-4.04e7	-4.02e7
mooring loads (N)	max	8.06e6	8.06e6	8.06e6	5.78e6
	min	-3.33e7	-3.36e7	-3.25e7	-2.66e7
	mean	-9.39e6	-9.35e6	-9.24e6	-9.26e6

3.3 Green Water

Under the present irregular wave condition, green water events occur on the CFPSO. The intensity and residence time of green water are analyzed for different scale ratios. Figs. 7, 8, and 9 illustrate the flow fields corresponding to the onset, the most intense stage, and the end of the green water event for different scale ratios, respectively. The time indicated in parentheses in each figure represents the corresponding instant converted to the full-scale condition. Among the four scale ratios, the onset times of green water for the 1:1, 1:20, 1:40, and 1:60 cases are 120 s, 118.51 s, 120.17 s, and 119.29 s, respectively. The most intense stages occur at 123 s, 122.98 s, 122.69 s, and 123.16 s, respectively, while the termination times are 128 s, 127.46 s, 127.12 s, and 127.81 s. Accordingly, the residence times of green water are approximately 8 s, 8.95 s, 6.95 s, and 8.52 s for the four scale ratios. These results indicate that the temporal sequence of green water occurrence remains generally consistent across different scale ratios, whereas noticeable differences exist in both the duration and intensity of the events. Among the considered cases, the 1:20 scale ratio exhibits the most intense green water with the longest residence time, while the 1:40 case shows the weakest green water response. The performances of the 1:1 and 1:60 cases are relatively close. This observation suggests that, although the occurrence time of green water is insensitive to scale variation, its development process and residence characteristics may still be influenced by scale-dependent nonlinear free-surface evolution and local inertial effects of the flow field, thereby altering the green water intensity and duration. Overall, the numerical simulations are capable of capturing the temporal characteristics of green water events reasonably well; however, scale effects should be taken into account in the quantitative evaluation of green water intensity and residence time.

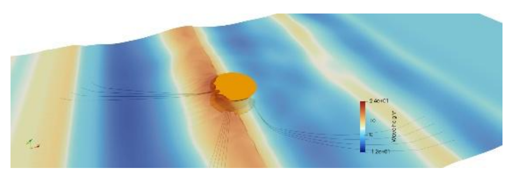
(a) 1:1 (120 s)

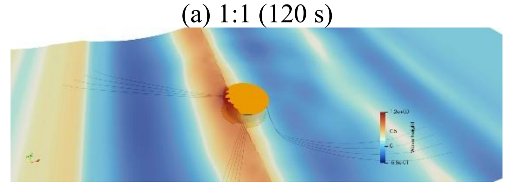
(b) 1:20 (118.51 s)

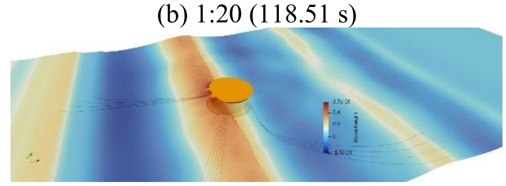
(c) 1:40 (120.17 s)

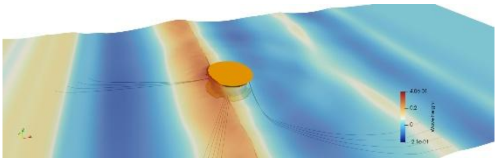

(d) 1:60 (119.29 s)

FIGURE 7: Flow field at the onset of green water for different scale ratios

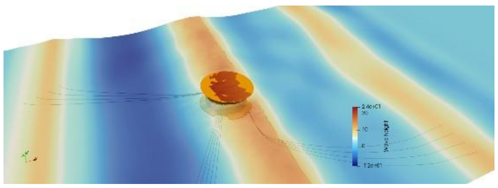

(a) 1:1 (123 s)

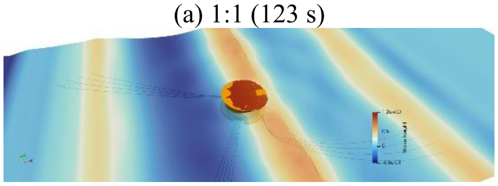

(b) 1:20 (122.98 s)

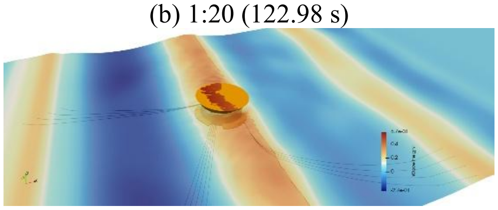

(c) 1:40 (122.69s)

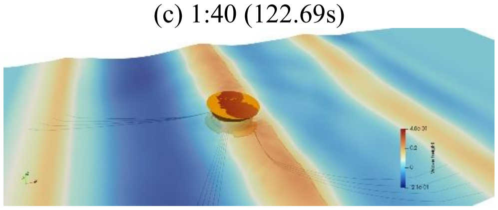

(d) 1:60 (123.16 s)

FIGURE 8: Flow field at the most intense stage of green water for different scale ratios

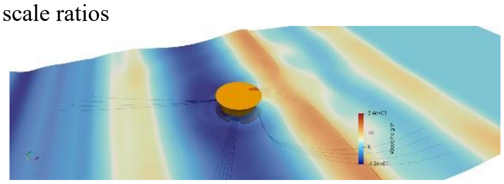

(a) 1:1 (128 s)

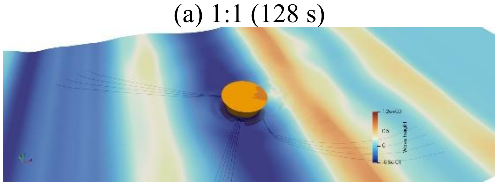

(b) 1:20 (127.46 s)

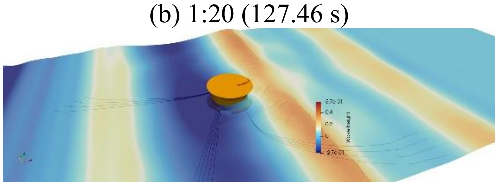

(c) 1:40 (127.12 s)

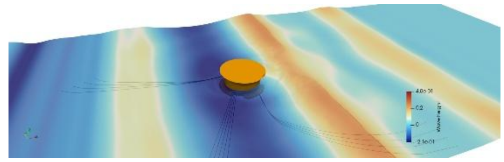

(d) 1:60 (127.81 s)

FIGURE 9: Flow field at the termination of green water for different scale ratios

3.4 Slamming Pressure

The arrangement of pressure probes on the CFPSO is illustrated in Fig. 10, and the coordinates of the pressure probes for the full-scale case are listed in Table 5. For convenience in comparative analysis, the pressure signals at all probes for different scale ratios are scaled to the full scale. Fig. 11 presents the time histories of wave-induced slamming pressure measured at each pressure probe for different scale ratios. The overall trends remain consistent among different scale ratios. The number of slamming events detected by the pressure probes decreases monotonically with increasing z-coordinate. Pressure probes located closer to the free surface are more prone to experiencing slamming events, whereas at higher vertical positions, the frequency of contact between the structure and incoming waves is reduced, resulting in a lower probability of slamming occurrence. At certain probes, negative slamming pressure values are observed, indicating a tendency for the fluid to detach from the structural surface and move outward. This behavior may be attributed to the separation of viscous flow from the structure surface prior to wave impact. In addition, the maximum slamming pressure for the smaller-scale cases (1:40 and 1:60) is approximately 3×10^5 Pa, whereas slightly higher maximum slamming pressures are observed for the larger-scale cases (1:20 and 1:1), reaching up to about 3.9×10^5 Pa.

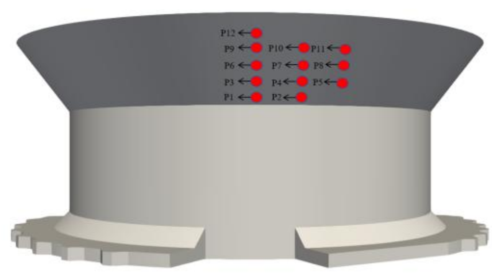

FIGURE 10: Schematic of pressure measurement probes on the CFPSO

TABLE 5: Coordinates of pressure measurement probes

No	x (m)	y (m)	z (m)
P1	-44.38	0	10
P2	-43.70	-7.70	10
P3	-46.29	0	12.5
P4	-45.59	-8.04	12.5
P5	-43.50	-15.83	12.5
P6	-48.20	0	15
P7	-47.47	-8.37	15
P8	-45.29	-16.48	15

P9	-50.12	0	17.5
P10	-49.35	-8.70	17.5
P11	-47.09	-17.14	17.5
P12	-52.26	0	20.3

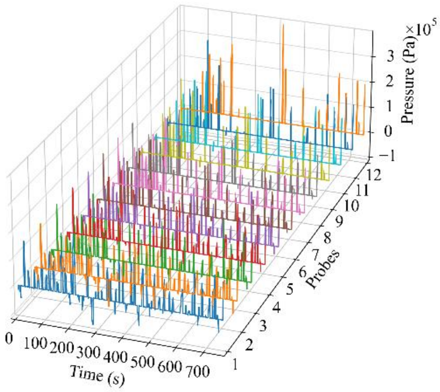

(a) 1:1

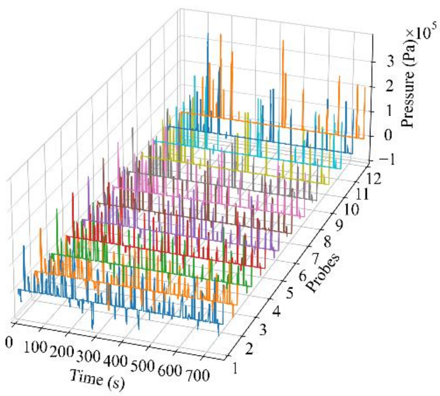

(b) 1:20

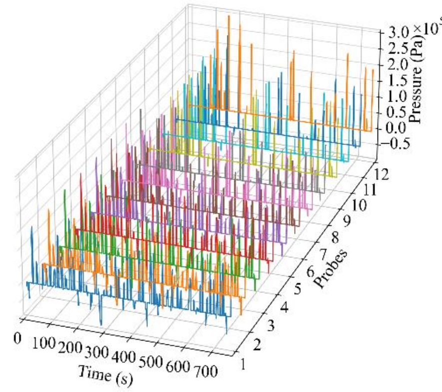

(c) 1:40

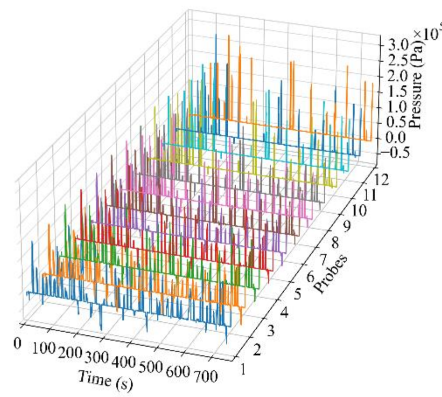

(d) 1:60

FIGURE 11: Time histories of slamming pressure at different pressure points for different scale ratios

Fig. 12 presents the pressure time histories at selected pressure probes for different scale ratios. It can be more clearly observed that the number of slamming events decreases with increasing vertical position of the pressure probes. In addition, a comparison among different scale ratios indicates that the occurrence time and frequency of slamming events remain generally consistent. For probes located at lower elevations, the differences in slamming pressure among different scale ratios are relatively small, whereas for probes at higher elevations, noticeably higher slamming pressures are observed for larger-scale cases compared with smaller-scale cases. Fig. 13 shows the pressure time histories in the vicinity of the instants when the maximum slamming pressure occurs at selected probes. The results more clearly demonstrate that the slamming pressures at probes P1, P3, and P6 are nearly identical across different scale ratios. In contrast, significant differences are observed at probes P9 and P12, where the slamming pressure increases with increasing scale ratio. For probes P9 and P12, the maximum slamming pressure differences between the 1:1 and 1:60 cases reach approximately 15% and 44%, respectively. These observations indicate that the scale effects on slamming pressure exhibit pronounced spatial non-uniformity. This behavior may be attributed to the fact that the slamming process at higher-elevation probes is closer to the critical state of free-surface coverage, making it more sensitive to small variations in green water intensity and transient free-surface morphology. Overall, it is observed that the scale effects on slamming pressure are spatially non-uniform. While the occurrence time and frequency of slamming events remain largely insensitive to scale variation, the magnitude of slamming pressure, particularly at higher-elevation probes, shows a clear dependence on scale.

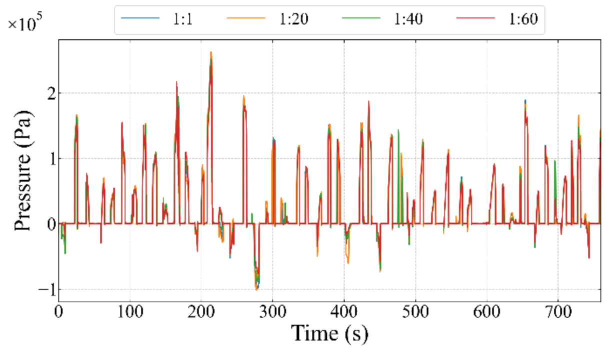

(a) P1

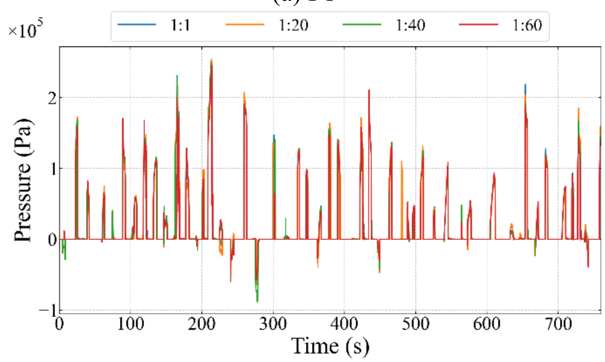

(b) P3

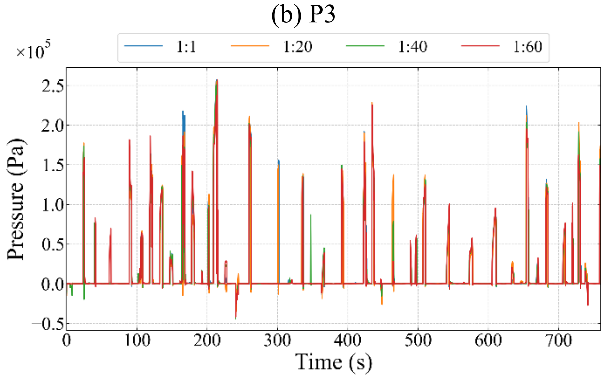

(c) P6

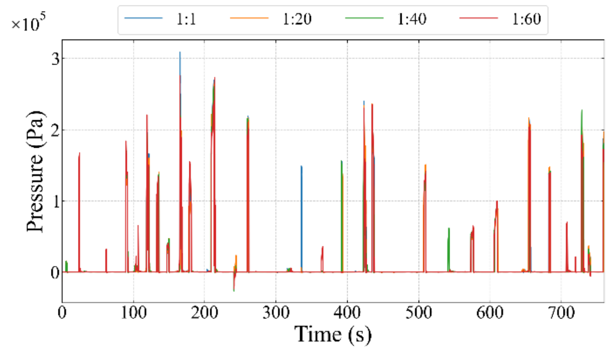

(d) P9

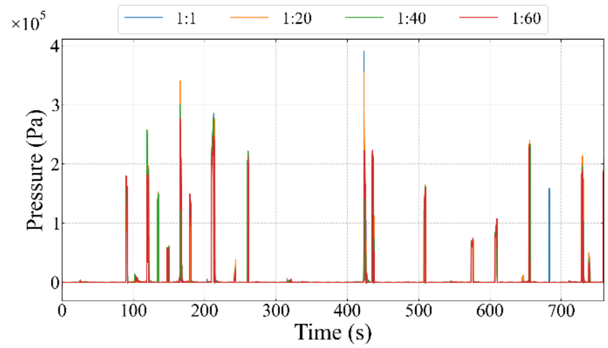

(e) P12

FIGURE 12: Pressure time histories at selected pressure probes for different scale ratios

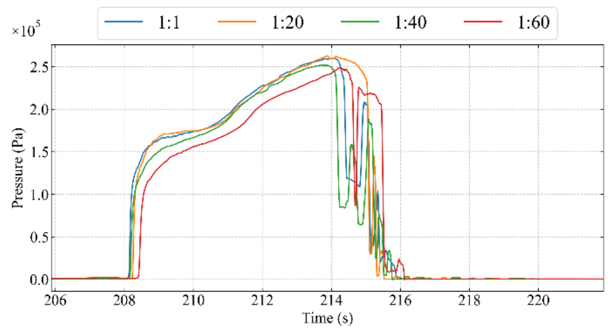

(a) P1

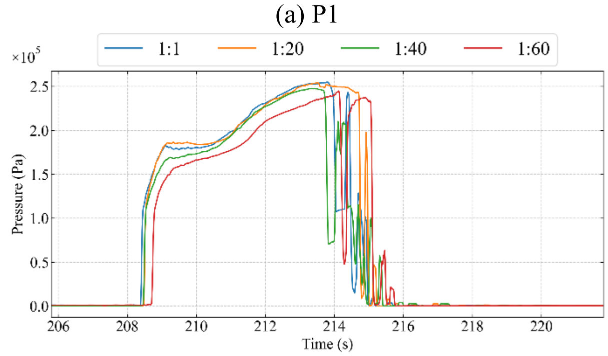

(b) P3

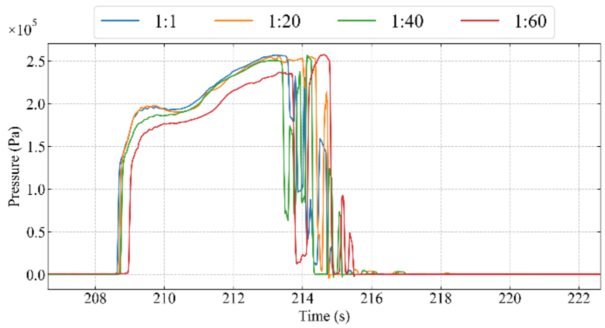

(c) P6

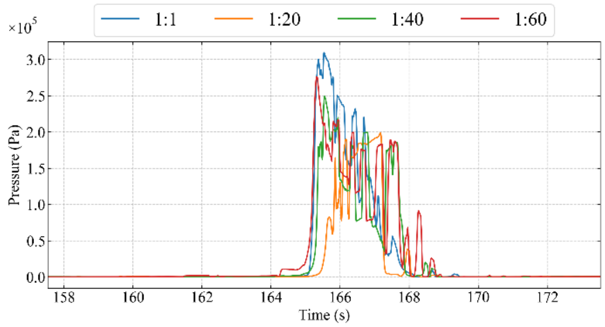

(d) P9

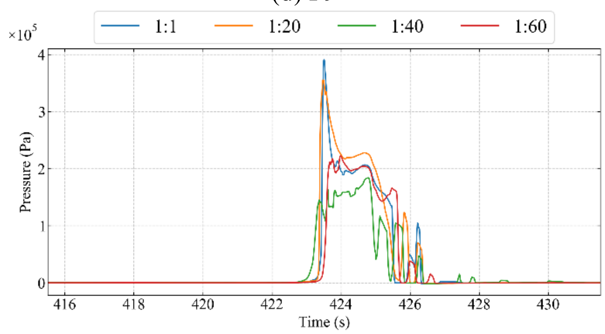

(e) P12

FIGURE 13: Pressure time histories near the instants of maximum slamming pressure at selected pressure probes for different scale ratios

4. CONCLUSION

In this study, CFD simulations are conducted to investigate the hydrodynamic responses of a CFPSO under irregular wave excitation at different scale ratios (1:1, 1:20, 1:40, and 1:60). Particular attention is paid to the scale effects on motion responses, horizontal loads, green water phenomena, and slamming pressure. Based on the numerical results, the following conclusions are drawn：

(1) From the comparison of motion responses and horizontal loads, it is found that, under irregular wave conditions, the overall evolution trends of motion responses and horizontal loads of the CFPSO remain consistent across different scale ratios. The differences in time-averaged motion responses and mean horizontal loads among different scales are relatively small, whereas noticeable discrepancies are observed in instantaneous responses and extreme values. In general, the instantaneous response amplitudes and load levels of larger-scale cases are slightly higher than those of smaller-scale cases. This indicates that, under the present wave conditions, motion responses and horizontal loads exhibit limited sensitivity to scale variation, although scale effects should still be considered when analyzing extreme responses.

(2) Based on the comparison of green water phenomena, it is observed that the temporal sequence of green water occurrence is generally consistent for different scale ratios, with good similarity in the onset, development, and termination stages. However, the intensity and residence time of green water show noticeable differences among different scales. The 1:20 scale case exhibits the most intense green water with the longest residence time, whereas the 1:40 case shows a relatively weaker response. These results indicate that the occurrence time of green water is insensitive to scale variation, while its development process and residence characteristics may still be influenced by scale-dependent nonlinear free-surface evolution.

(3) A comparison of slamming phenomena reveals that the occurrence frequency and temporal distribution of slamming events remain generally similar among different scale ratios. However, the magnitude of slamming pressure exhibits significant differences across scales, particularly at high-elevation probes away from the free surface, where larger-scale cases produce clearly higher slamming pressures than smaller-scale cases. This indicates that slamming pressure is more sensitive to scale variation.

Overall, under the irregular wave conditions considered in this study, the global motion responses, horizontal loads, and the temporal sequence of green water events of the CFPSO exhibit good similarity across different scale ratios, while scale effects are mainly manifested in instantaneous extreme responses, green water intensity, and slamming pressure. The findings of this study provide a useful reference for the assessment of scale effects of CFPSOs in engineering applications. It should be noted that the present simulations adopt the laminar-flow setting, which has been shown to better preserve the target wave-elevation characteristics within the adopted two-phase wave-generation framework. Nevertheless, this assumption does not explicitly resolve turbulence-related dissipation effects and small-scale vortical structures, which may influence highly localized processes. Further work will consider turbulence modeling to quantify its influence on green-water and slamming-pressure predictions. It is also noted that the simulated physical time is constrained by the high computational cost of high-fidelity two-phase CFD under irregular waves; future work will explore longer-duration assessments using more efficient approaches (e.g., potential-flow method) and benchmark key statistics against the present CFD results.

ACKNOWLEDGEMENTS

This work was supported by the National Natural Science Foundation of China (52131102).

REFERENCES

[1] Seok W., Park S. Y., Rhee S. H. An experimental study on the stern bottom pressure distribution of a high-speed planing vessel with and without interceptors[J]. *International Journal of Naval Architecture and Ocean Engineering*. 2020, 12: 691–698.

[2] Amin I., Dai S., Day S., et al. Experimental investigation on the influence of interceptor plate on the motion performance of a cylindrical FPSO[J]. *Ocean Engineering*. 2022, 243: 110339.

[3] Gu, J, Xie, Y, Zhang, P, et al. Experimental study on hydrodynamic performance of a new type of deep draft multi-column FDPSO[J]. *Journal of Marine Science and Technology*. 2017, 25(3).

[4] Deng S., Cai Y., Yang X., et al. Experimental Study on the Effects of Wave and Current Interaction on Vertical Motions of a Cylindrical FPSO[C]. *The 32nd International Ocean and Polar Engineering Conference*. 2022: ISOPE-I-22-172.

[5] Deng S., Zhong W., Yang X., et al. Experimental and numerical study of the hydrodynamic features of a cylindrical FPSO considering current-induced motion[J]. *Ocean Engineering*. 2022, 262: 112263.

[6] Cui Y., Li Y., Li G., et al. Dynamic response and nonlinear resonance of cylindrical FPSO with a ring groove considering time-varying restoring stiffness[J]. *Ocean Engineering*. 2025, 325: 120857.

[7] Avalos G. O. G., Wanderley J. B. V. Numerical study of forced roll oscillation of FPSO with bilge keel[J]. *Ocean Engineering*. 2018, 147: 304–317.

[8] Jiang M., Li D., Wang Z., et al. Hydrodynamic Study on the Damping Characteristics of Cylindrical FPSO With the Heave Plate[C]. Volume 1: Offshore Technology, 2020.

[9] Huo S., Deng S., Song Z., et al. On the hydrodynamic response and slamming impact of a cylindrical FPSO in combined wave-current flows[J]. *Ocean Engineering*. 2023, 275: 114139.

[10] Zhao W., Yang X., Wan D. Numerical analysis of coupled sloshing and motion of a cylindrical FPSO in regular waves[J]. *Journal of Hydrodynamics*. 2024, 36(3): 457–465.

[11] Terziev M., Tezdogan T., Incecik A. Scale effects and full-scale ship hydrodynamics: A review[J]. *Ocean Engineering*. 2022, 245: 110496.

[12] Wang J., Wang W., Wan D. Scale effects on bow wave breaking of KCS ship model: Insights from DDES investigations[J]. *Journal of Hydrodynamics*. 2023, 35(4): 668–678.

[13] Liu B., Vanierschot M., Buysschaert F. Numerical study of scale effects on the open water performance of a rim-driven thruster[J]. *Applied Ocean Research*. 2023, 138: 103667.

[14] Chen Z., Jiao J., Jiang C., et al. Scale effects on wave loads and slamming loads in ship hydroelasticity simulation by CFD-FEM method[J]. *Ocean Engineering*. 2024, 314: 119718.

[15] Wang J., Zhao W., Wan D. Development of naoe-FOAM-SJTU solver based on OpenFOAM for marine hydrodynamics[J]. *Journal of Hydrodynamics*. 2019, 31(1): 1–20.

[16] Shen Z., Wan D. RANS Computations of Added Resistance and Motions of a Ship in Head Waves[J]. *International Journal of Offshore and Polar Engineering*. 2014, 23(04): 264–271.

.